Anomalous spin dynamics of the $S = \frac{3}{2}$ kagome ferromagnet $Li_9Cr_3(P_2O_7)_3(PO_4)_2$

G. Senthil Murugan,[1,*] Chanhyeon Lee,[2,*] R. Kalaivanan,[1] I. Panneer Muthuselvam,[3] Yugo Oshima,[4] Kwang-Yong Choi,[5,†] and R. Sankar[1,‡]

[1]*Institute of Physics, Academia Sinica, Taipei 10617, Taiwan*
[2]*Department of Physics, Chung-Ang University, Seoul 06974, Republic of Korea*
[3]*Department of Physics (MMV), Banaras Hindu University, Varanasi 221005, Uttar Pradesh, India*
[4]*Meson Science Laboratory, RIKEN Cluster for Pioneering Research, Hirosawa 2-1, Wako, Saitama 351-0198, Japan*
[5]*Department of Physics, Sungkyunkwan University, Suwon 16419, Republic of Korea*

(Received 17 January 2023; revised 25 May 2023; accepted 25 May 2023; published 8 June 2023)

We report the dynamical magnetic properties of the $s = \frac{3}{2}$ kagome ferromagnet $Li_9Cr_3(P_2O_7)_3(PO_4)_2$ using magnetic susceptibility, specific heat, electron spin resonance (ESR), and nuclear magnetic resonance techniques. The magnetic susceptibility and specific heat show ferromagnetic ordering at $T_C = 2.7$ K. The in-plane ferromagnetic correlation length ξ_{ab} deduced from the magnetization curves reveals that ξ_{ab} increases steeply from 18.2 to 41.3 Å as the temperature is lowered from 50 K to T_C, indicative of the persistence of two-dimensional magnetic correlations up to temperatures as high as $\sim 18\,T_C$. The ESR linewidth ΔH_{pp} and magnetic specific heat data indicate a change in spin dynamics at about $T^* \approx 4.4T_C$. Intriguingly, for temperatures below 50 K, we observe an unexpected suppression of the ^{7}Li spin-lattice relaxation rate $1/T_1$. The decrease in $1/T_1$, which occurs well above T_C, is at odds with the critical slowing down of magnetic correlations typically observed in conventional ferromagnets. This anomalous thermal evolution of spin fluctuations is interpreted in terms of the concerted interplay of flat and Dirac magnon bands inherent in kagome ferromagnets.

DOI: 10.1103/PhysRevB.107.214411

I. INTRODUCTION

Recently, topological magnon insulators, bosonic analogs of electronic topological insulators, have garnered fundamental interest because they provide a prominent platform for exploring topological phases and phenomena of charge-neutral bosonic quasiparticles [1,2]. Chern magnon bands have far-reaching ramifications in heat and spin transport as well as in magnon dynamics.

In particular, the presence of topologically protected magnon edge modes within a bulk band gap can give rise to the magnon Hall effect [3–7]. The Dzyaloshinskii-Moriya interaction, acting as an effective spin-orbit coupling for magnons, opens gaps at finite energies in the spin-wave spectrum and leads to a finite Berry curvature. The Berry curvature of magnon bands induces a transverse magnon current perpendicular to an applied temperature gradient. A number of theoretical models for achieving topologically nontrivial magnon bands and the thermal Hall effect have been proposed in diverse systems based on different types of spin lattices, such as honeycomb ferromagnets, triangular antiferromagnets, noncollinear or noncoplanar kagome antiferromagnets, and kagome ferromagnets [8–17]. Experimental evidence for the predicted magnon Hall effect has been reported for the pyrochlore ferromagnet $Lu_2V_2O_7$, kagome ferromagnet Cu(1,3-bdc), and honeycomb antiferromagnet $Na_2Co_2TeO_6$ [18–23].

Among different spin lattices, the kagome ferromagnets provide a unique setting to investigate the behavior of flat bands, Dirac fermions, topological phase transitions, and novel topological excitations [24–26].

$Li_9Cr_3(P_2O_7)_3(PO_4)_2$ (trigonal space group $P\bar{3}c1$), abbreviated as LCPP, is a rare example of $s = \frac{3}{2}$ kagome ferromagnets [27]. As shown in Figs. 1(a) and 1(b), corner-sharing equilateral triangles of Cr^{3+} ($3d^3$) ions form a kagome lattice, in which CrO_6 octahedra share corners with PO_4 tetrahedra and P_2O_7 polyhedra in the *ab* plane. The adjacent kagome planes are well separated by Li^+ ions. Magar *et al.* [28] extensively characterized the magnetic properties of LCPP. By employing density functional theory calculations and analyzing magnetic susceptibility, they determined that the nearest-neighbor intralayer ferromagnetic (FM) exchange coupling is approximately $J/k_B = -1.2$ K, while the small interlayer coupling is $\sim 2\%$ of J, which stabilizes the FM ordering at $T_C \approx 2.6$ K. The magnetic entropy is partially released at T_C, and the broadening of the electron spin resonance (ESR) line persists well above T_C, indicating the quasi-two-dimensional (quasi-2D) nature of magnetic correlations. In addition, the large magnetocaloric effect observed around T_C renders the material a potential candidate for magnetic refrigeration. Despite identifying quasi-2D spin dynamics, not much is known about the relationship between spin correlations and the inherent topological magnon bands in kagome ferromagnets.

*These authors contributed equally to this work.
†choisky99@skku.edu
‡sankarndf@gmail.com

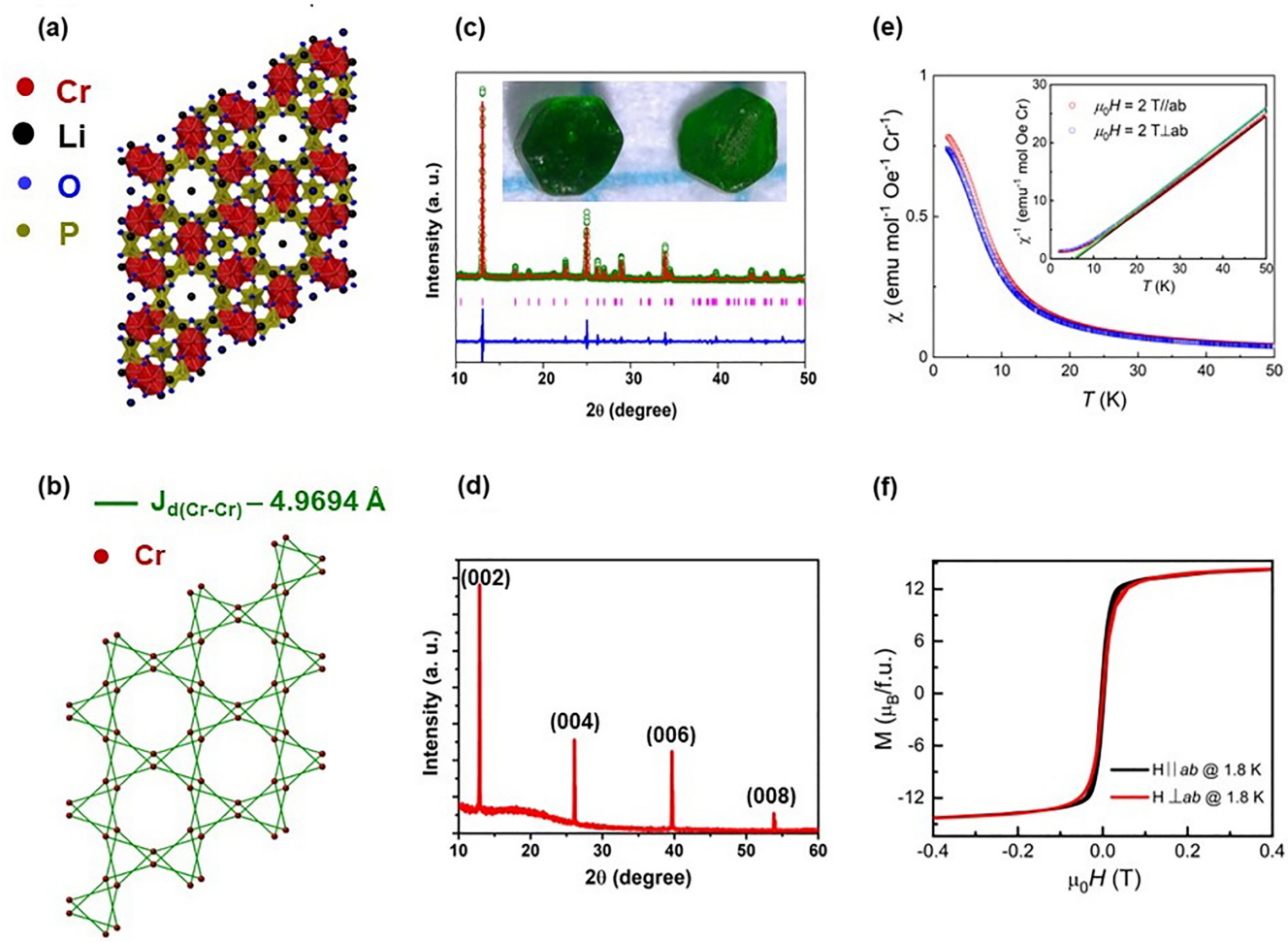

FIG. 1. (a) Crystal structure of $Li_9Cr_3(P_2O_7)_3(PO_4)_2$ (LCPP). CrO_6 octahedra share the corners with PO_4 tetrahedra and P_2O_7 polyhedra in the *ab* plane, and the Li atoms lie between the layers. (b) Cr^{3+} spins form kagome layers in the *ab* plane that are slightly rotated by a small angle. (c) Rietveld refinement of the x-ray diffraction pattern for LCPP. The observed data, Rietveld refinement fit, Bragg peaks, and difference curve are denoted by the green open circles, red solid line, blue solid line, and vertical magenta dashes, respectively. The inset shows a photo of LCPP single crystals. (d) XRD pattern with (00L) orientation. (e) Temperature dependence of the dc magnetic susceptibilities of LCPP for $H \parallel ab$ and $H \perp ab$ in an applied field of $\mu_0 H = 2$ T. The inset shows the $1/\chi$ plot. The red solid line represents the Curie-Weiss law. (f) Magnetization curves of LCPP measured at $T = 1.8$ K for two field orientations, $H \parallel ab$ and $H \perp ab$.

Herein, we investigate the dynamical magnetic properties of the $s = \frac{3}{2}$ kagome FM material LCPP by combining thermodynamic and magnetic resonance techniques. Magnetization, ESR, and ^{7}Li NMR reveal that FM correlations persist up to 50 K, which corresponds to approximately $18T_C$. Interestingly, we observe an unexpected decrease of the ^{7}Li spin-lattice relaxation rate $1/T_1$ below $18T_C$ (in a paramagnetic state). Additionally, we identify a crossover of the ESR linewidth and a broad hump of the magnetic specific heat at about $T^* \approx 12$ K ($\approx 4.4T_C$). These findings demonstrate the significant role of flat magnon bands in inducing intriguing short-range spin dynamics.

II. EXPERIMENTAL DETAILS

To grow single crystals of $Li_9Cr_3(P_2O_7)_3(PO_4)_2$, a mixture of $LiCO_3$, Cr_2O_3, and $NH_4H_2PO_4$ (99.95% purity) was thoroughly ground and placed in a platinum crucible. First, the mixture was heated at 300 °C and 600 °C in the air for 12 h each (with a heating rate of 100 °C/h), with intermediate grindings. Next, the preheated sample was reground and heated at 950 °C for 24 h with a heating rate of 100 °C/h. Then, the furnace was cooled down to 850 °C, 750 °C, and 650 °C, each with a cooling rate of 1°C/h, and finally cooled down to room temperature with a cooling rate of 100 °C/h. The resulting single crystals were separated from the crucible and subsequently washed with hot water. The inset of Fig. 1(c) shows the hexagonal, green-colored single crystals of LCPP.

To check the phase purity of the grown crystal, we recorded an x-ray diffraction (XRD) at room temperature. Crushed crystal powder was used for the XRD measurement. The data were analyzed by Rietveld analysis using the FULLPROF package. Figures 1(c) and 1(d) display the XRD pattern of Rietveld refinement for a pulverized LCPP single crystal and the XRD pattern for the

preferred (00L) orientation of the LCPP single crystal, respectively. We obtain the refined lattice parameters $a = 9.6692(3)$ Å, $c = 13.5862(8)$ Å, and $V = 1100.03(8)$ Å^3, which are consistent with the literature [27,28]. The refinement yields a goodness of fit, $R_p = 12.15\%$, $R_{wp} = 16.53\%$, $R_{exp} = 7.55\%$, and $\chi^2 = 4.78$.

Magnetic measurements were performed using a superconducting quantum interference device vibrating-sample magnetometer (Quantum Design, USA). The specific heat was measured using a physical property measurement system (Quantum Design, USA) with the standard relaxation method. For ESR experiments, we used a conventional X-band ESR system (JEOL JES-RE3X). The ESR signals were recorded by sweeping an external field at a fixed frequency of $\nu = 9.12$ GHz. The temperature is varied between 3.6 and 300 K using a continuous He flow cryostat (ESR 900, Oxford Instruments).

^{7}Li ($I = 3/2$ and $\gamma_N = 16.5471$ MHz/T) nuclear magnetic resonance (NMR) experiments were conducted using a MagRes spectrometer (developed at National High Magnetic Field Laboratory, USA) and a 14 T Oxford Teslatron PT superconducting magnet. An external magnetic field of $\mu_0 H = 2$ T was applied parallel to the ab plane of the single LCPP crystal. The ^{7}Li NMR spectra were acquired using a standard Hahn-echo method with a $\pi/2$ pulse length of 1.5–2 μs. To study the low-energy spin dynamics of Cr^{3+} spins, we measured the spin-lattice relaxation rate $1/T_1$ versus temperature by employing the saturation recovery technique with double saturation pulses. In our analysis, we fitted the nuclear magnetization recovery curve $M(t)$ with both a conventional stretched exponential function $M(t) = M_\infty[1 - \exp(-t/T_1^{str})^\beta]$, where β is the stretching exponent, and the inverse Laplace transform (ILT) method based on Tikhonov regularization [29,30].

III. RESULTS AND DISCUSSION

A. Magnetic susceptibility and specific heat

Figure 1(e) presents the temperature dependence of the dc magnetic susceptibility $\chi(T)$ of LCPP single crystals measured in an external field of $\mu_0 H = 2$ T. The rather high external field is applied for comparison with the NMR shift (see Sec. III D). Upon cooling down to 1.8 K, $\chi(T)$ steeply increases, indicative of the development of FM correlations and eventual FM ordering at $T_C \sim 2.7$ K [see the inset of Fig. 2(a)]. In the high-temperature paramagnetic regime ($T =$ 20–300 K), the $\chi(T)$ data follow the Curie-Weiss (CW) behavior $\chi(T) \sim C/(T - \Theta)$, as shown in the $1/\chi$ plot in the inset of Fig. 1(e). From the CW fitting, the effective magnetic moment and the CW temperature are evaluated to be $\mu_{eff} = 3.81\mu_B/Cr^{3+}$ and $\Theta = 5.49$ K for $H \parallel ab$, respectively, and $\mu_{eff} = 3.75\,\mu_B/Cr^{3+}$ and $\Theta = 5.05$ K for $H \perp ab$. The positive Θ indicates dominant FM interactions between the Cr^{3+} spins. The extracted effective magnetic moments are slightly smaller than the expected spin-only value of $\mu_{cal} = 3.87\mu_B/Cr^{3+}$.

To gain more insight into the magnetic properties of the LCPP single crystal, we further measured the field dependence of magnetization $M(H)$ along $H \parallel ab$ and $H \perp ab$ at 1.8 K. The results are presented in Fig. 1(f) after correcting anisotropic demagnetization effects (the demagnetization factor $N = 0.88$ for $H \perp ab$). The in-plane $M(H)$ saturates at a slightly lower field than the out-of-plane $M(H)$. This coincides with a previous study [28] which revealed that LCPP is a ferromagnet with a small easy-plane anisotropy.

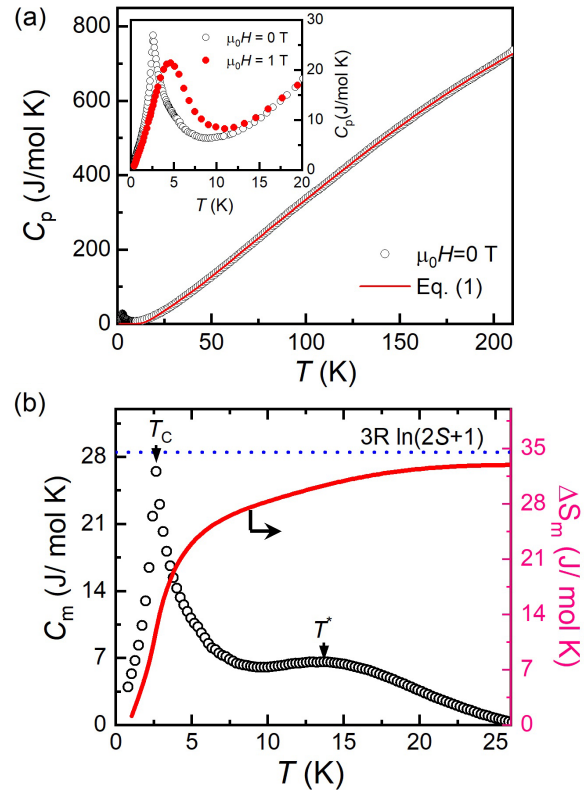

FIG. 2. (a) Temperature dependence of the specific heat $C_p(T)$ for a $Li_9Cr_3(P_2O_7)_3(PO_4)_2$ single crystal measured in zero field. The red solid line represents the phonon contribution calculated using the combined Debye and Einstein model. The inset compares the low-temperature $C_p(T)$ data between 0 and 1 T. (b) The magnetic specific heat C_{mag} (black circles) and the spin entropy change ΔS_m (red line) as a function of temperature. The horizontal dotted line indicates a theoretical value of the total magnetic entropy. The vertical arrows mark the magnetic transition and crossover.

Figure 2(a) presents the temperature dependence of the specific heat $C_p(T)$ of LCPP. In the absence of an applied magnetic field, we observe a λ peak at $T_C = 2.7$ K, confirming the FM ordering. With increasing applied field, the peak broadens and shifts to higher temperatures, as shown in the inset Fig. 2(a). The broad maximum points to a transition to a FM polarized state. The red solid line denotes the lattice contribution $C_{ph}(T)$ to the total specific heat. The magnetic specific heat $C_m(T)$ is separated by subtracting $C_{ph}(T)$ from $C_p(T)$. To estimate the C_{ph} contribution, we fitted the C_p data to a combination of one Debye and two Einstein terms as [31]

$$C_{ph}(T) = f_D C_D(\theta_D, T) + \sum_{i=1}^{2} g_i C_E(\theta_i, T). \quad (1)$$

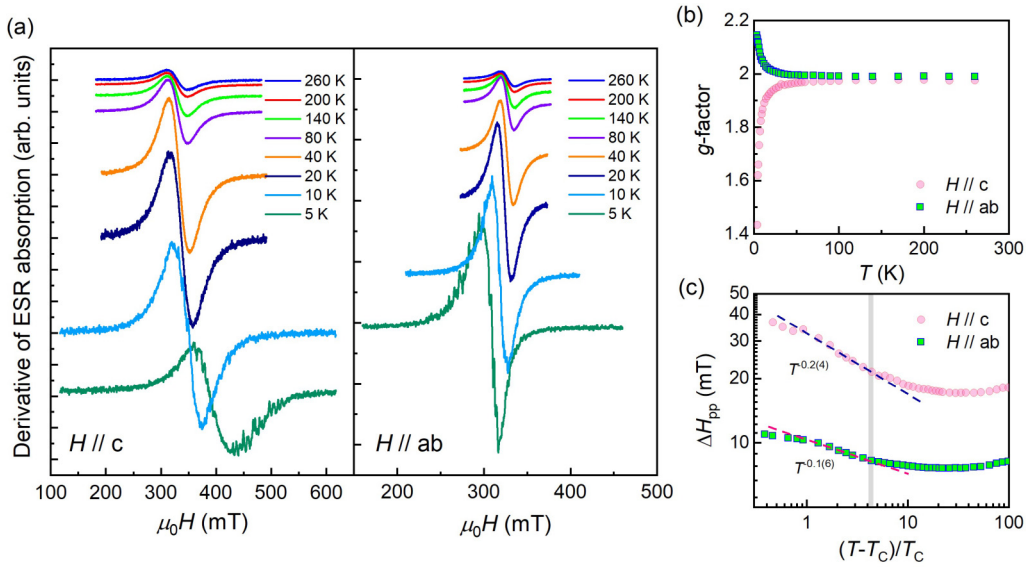

FIG. 3. (a) Derivative of the ESR absorption spectra at selected temperatures for $H \parallel c$ and $H \parallel ab$. (b) Temperature dependence of the g factors for $H \parallel c$ (pink circles) and $H \parallel ab$ (green squares). (c) Log-log plot of the peak-to-peak linewidth ΔH_{pp} as a function of the reduced temperature. The dashed lines are power-law fits. The gray shading marks the onset temperature of the critical increase of ΔH_{pp}.

The Debye and Einstein terms are given as

$$C_D(\theta_D, T) = 9nR\left(\frac{T}{\theta_D}\right)^3 \int_0^{\frac{\theta_D}{T}} \frac{x^4 e^x}{(e^x-1)^2} dx,$$

$$C_E(\theta_E, T) = 3nR\left(\frac{\theta_E}{T}\right)^2 \frac{e^{\frac{\theta_E}{T}}}{\left(e^{\frac{\theta_E}{T}}-1\right)^2}, \quad (2)$$

where $x = \frac{\hbar\omega}{k_B T}$ with a vibration frequency ω, $R = 8.314$ J/(mol/K) is the universal gas constant, and θ_D and θ_E are the characteristic Debye and Einstein temperatures, respectively. Fitting the $C_p(T)$ data to Eq. (1) in the $T = 23$–210 K range yields the following fitting parameters: $\theta_D = 904.(8)$ K, $\theta_{E1} = 102.(7)$ K, and $\theta_{E2} = 275.(0)$ K and the weight factors $f_D = 0.69(5)$, $g_1 = 0.09(7)$, and $g_2 = 0.20(8)$.

The low-temperature $C_m(T)$ data are plotted in Fig. 2(b). In addition to the λ-like peak at T_C, a broad hump is discernible at $T^* \approx 13$ K, alluding to the presence of emergent spin correlations above T_C. We further calculate the spin entropy change ΔS_m by integrating C_m/T with respect to temperature ($\Delta S_m = \int \frac{C_m}{T} dT$). As shown on the right axis of Fig. 2(b), a spin entropy of 12.38 J/(mol/K) is released below $T_C = 2.7$ K, which corresponds to ∼37.5% of the total spin entropy 33.03 J/(mol/K) [close to the theoretical total spin entropy $3R\ln(2S+1) = 34.58$ J/(mol/K) for $s = \frac{3}{2}$]. The remaining ∼62.5% of ΔS_m is released between T_C and 26 K. This demonstrates that short-range correlations persist at least up to 26 K. It is noteworthy that the same conclusion is drawn from the specific heat study reported previously in Ref. [28].

B. ESR

To obtain information about the thermal evolution of spin correlations, we conducted X-band ESR measurements. Figure 3(a) shows the selected ESR spectra in the $T = 3.6$–260 K range for $H \parallel c$ and $H \parallel ab$, respectively. All the measured ESR spectra are well described by a single Lorentzian profile, implying that the ESR signals are exchange narrowed due to the fast electronic fluctuations of the Cr^{3+} spins.

With decreasing temperature to 3.6 K, the ESR signal broadens progressively and shifts to higher (lower) fields for $H \parallel c$ ($H \parallel ab$). For quantitative analysis, the ESR absorption lines were fitted to the derivative of a Lorentzian profile. The resulting parameters are plotted against temperature in Figs. 3(b) and 3(c). At $T = 260$ K, the effective g factors are evaluated to be $g_{ab} = 1.99$ and $g_c = 1.97$, which are comparable to $g_{ab} = 1.968 \pm 0.003$ and $g_c = 1.958 \pm 0.003$ determined by multifrequency FM resonance measurements [28]. The slightly anisotropic g tensor, being smaller than the free spin value of $g = 2.0023$, is typical for a less-than-half-filled Cr^{3+} ion with a negligible spin-orbit interaction in an octahedral ligand coordination [32,33]. On cooling from 50 K, g_{ab} increases rapidly towards 2.14 as $T \to T_C$, while g_c shows a substantial decrease to 1.43. The positive shift of g_{ab}, corresponding to a negative shift of the resonance field for $H \parallel ab$, is consistent with an easy-plane ferromagnet.

Figure 3(c) exhibits the peak-to-peak linewidth ΔH_{pp} as a function of reduced temperature, $T_r \equiv (T - T_C)/T_C$, on a log-log scale. In the simple paramagnetic regime above 50 K, $\Delta H_{pp}(T)$ is largely independent of temperature. As the temperature is lowered from 50 K, however, $\Delta H_{pp}(T)$ shows a weak increase, indicating the development of magnetic correlations. Upon cooling through $T^* = 12$ K (∼$4.4T_C$), the critical increase of ΔH_{pp} is described by the power-law form $\Delta H_{pp}(T) \sim T_r^{-p}$, with exponents of $p = 0.2(4)$ for $H \parallel c$ and $p = 0.1(6)$ for $H \parallel ab$. The critical exponent p is related to the spatial decay of static correlations, depending on dimensionality. On approaching T_C, the critical slowing down diminishes, leading to deviations from the power-law behavior. The change from the smooth increase to the

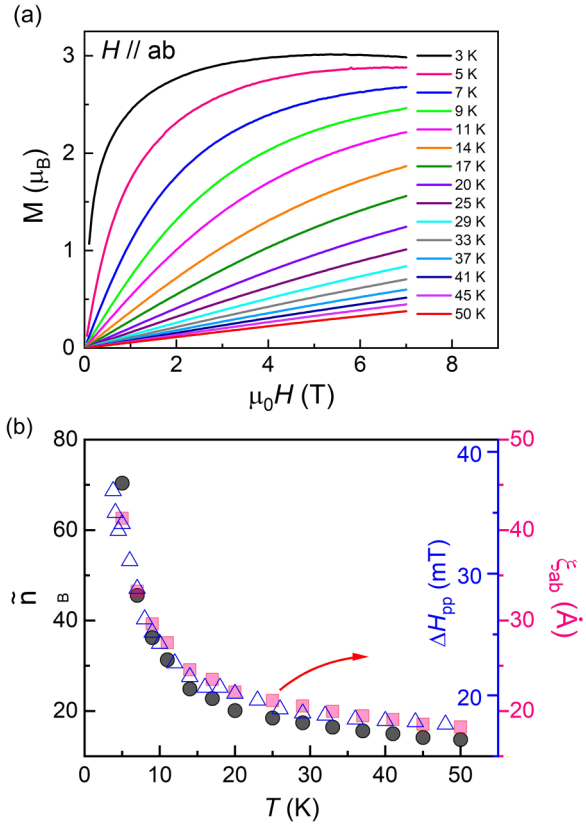

FIG. 4. (a) Temperature and field dependence of magnetization curves for $H \parallel ab$ scaled by $M_S = gS\mu_B$ for each temperature. (b) Temperature dependence of the number of ferromagnetically correlated moments $\tilde{n}$ (black circles; left axis), the ferromagnetic correlation length ξ_{ab} (pink squares; pink right axis), and the ESR linewidth ΔH_{pp} (open triangles; blue right axis).

critical broadening through T^* is of pure magnetic origin since the absence of g factor anomaly excludes a structural distortion. Overall, the larger exponent of the out-of-plane $\Delta H_{pp}(T)$ is associated with the augmentation of critical fluctuations due to interlayer couplings or easy-plane anisotropy. Furthermore, the concurrent critical line broadening and the g factor shift evidence the persistence of short-range spin correlations as high as $18T_C$, generic to low-dimensional quantum magnets. Essentially the same behavior has also been observed in the high-frequency ESR experiment [28]. Compared to other 2D systems [34], the small exponent p observed in LCPP, together with the persistence of magnetic correlations to very high temperatures, suggests the significance of localized spin correlations inherent in kagome ferromagnets [21].

C. Thermal evolution of magnetic correlation length

Figure 4(a) presents the magnetization curves $M(H,T)$ measured in the temperature range below $T = 50$ K. The $M(H,T)$ curves are scaled to the expected saturation values $M_S^{ab} = g_{ab}S\mu_B$. As inferred from the ESR data, FM correlations start to develop at 50 K. As such, we attempt to describe the $M(H,T)$ curves as the sum of a modified Brillouin function $B_{\tilde{S}}$ and a linearly increasing term:

$$M(H,T) = M_S B_{\tilde{S}}\left(\frac{g\mu_B \tilde{S} B}{k_B T}\right) + \chi_0 B, \tag{3}$$

where $\tilde{S}$ is the effective spin of the correlated cluster and χ_0 is a field-independent contribution to magnetic susceptibility. From the obtained $\tilde{S}$, we can determine the number of ferromagnetically correlated Cr^{3+} moments, $\tilde{n} = \tilde{S}/S$. As shown in the solid circles in Fig. 4(b), $\tilde{n}$ rapidly increases as the temperature is decreased from $T = 50$ to 5 K. Assuming a homogeneous distribution of $\tilde{n}$ correlated spins in the ab plane, the FM correlation length ξ_{ab} can be evaluated as $\xi_{ab} = \sqrt{(2\sqrt{3}d^2/\pi)\tilde{S}}$ [35], where the distance between the nearest-neighbor Cr^{3+} spins is $d(\mathrm{Cr}-\mathrm{Cr}) = 4.9694$ Å, as depicted by the green lines in Fig. 1(b). The resulting ξ_{ab} (pink squares) is plotted together with the ESR linewidth ΔH_{pp} (open blue triangles) as a function of temperature in Fig. 4(b). It is found that $\xi_{ab} \simeq 18.2$ Å at 50 K increases towards $\xi_{ab} \simeq 41.3$ Å as the temperature approaches 5 K. It is worth noting that the $s = \frac{1}{2}$ kagome ferromagnet $\alpha - MgCu_3(OD)_6Cl_2$ and van der Waals ferromagnet CrI_3 display a similar thermal evolution of in-plane magnetic correlation length well above T_C [36,37]. Furthermore, we find a close overlap between the ESR linewidth ΔH_{pp} and the correlation length ξ_{ab}, which relies on the fact that the critical broadening ESR linewidth is associated with the spatial decay of the static spin correlations.

D. ^{7}Li NMR

The temperature dependence of the ^{7}Li NMR spectra of LCPP is shown in Fig. 5(a). The crystal is oriented in a field direction parallel to the ab plane. We observe two NMR lines labeled P1 and P2, which are closely spaced. Since LCPP contains three crystallographically different Li sites, we normally expect to observe three NMR peaks. Nonetheless, we note that the distances between the Cr and Li sites are given by d_1(Cr-Li I) = 5.39167 Å, d_2(Cr-Li II) = 3.38010 Å, and d_3(Cr-Li III) = 3.02599 Å. The 2:1 intensity ratio between the P1 and P2 peaks, combined with the comparable distances between the Cr and Li II/Li III sites, indicates an overlap of the Li II/Li III resonance lines within the P1 peak. Although this qualitative argument offers a plausible explanation for the two observed NMR lines, we admit that a sophisticated quantum mechanical method is required to accurately compute the hyperfine tensor and NMR line shift. Moreover, the ^{7}Li ($I = 3/2$) NMR spectrum generically consists of three resonance lines: a pair of satellite resonance lines ($|-\frac{3}{2}\rangle \longleftrightarrow |-\frac{1}{2}\rangle$, $|\frac{1}{2}\rangle \longleftrightarrow |\frac{3}{2}\rangle$) and a central resonance line ($|-\frac{1}{2}\rangle \longleftrightarrow |\frac{1}{2}\rangle$). In the case of LCPP, the quadrupole splitting between the central and satellite resonance lines is estimated to be $\Delta\nu = \nu_C - \nu_Q < 0.2$ MHz, which is smaller than the linewidth of our NMR spectrum. This small quadrupole splitting accounts for the unresolved satellite lines.

With decreasing temperature, the NMR peaks shift toward higher fields, while their linewidth gradually increases. The line shift and broadening concur with the development of long-range magnetic ordering towards T_C. The relative shift of the NMR line stems from the local magnetic fields and is quantified by $K = (\nu_{peak} - \nu_0)/\nu_0 \times 100$ (%), where

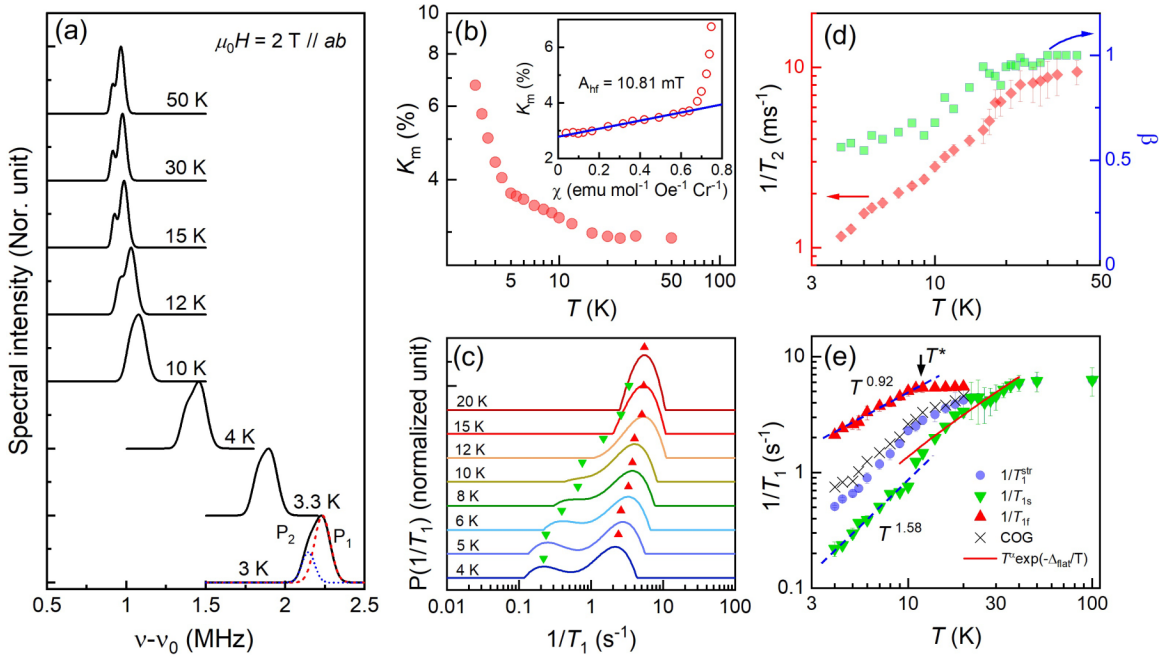

FIG. 5. (a) ^{7}Li NMR spectra of LCPP measured at $\mu_0 H = 2\,\mathrm{T} \parallel ab$. (b) Temperature dependence of the magnetic shift $K_m(T)$ of the ^{7}Li nuclear spins. The inset plots the temperature dependence of the magnetic shift versus dc susceptibility. The solid line is the Clogston-Jaccarino plot as described in the text. (c) Distribution function $P(1/T_1)$ as a function of temperature. The symbols mark two components of $1/T_1$: $1/T_{1s}$ (green inverted triangles) and $1/T_{1f}$ (pink triangles). (d) Temperature dependence of the spin-spin relaxation rate $1/T_2$ (left axis) and the stretched exponent β (right axis). (e) Log-log plot of the ^{7}Li spin-lattice relaxation rates $1/T_{1s}$, $1/T_{1f}$, and T_1^{str} along with the center of gravity (COG). The dashed lines are fits to the power-law dependence $1/T_1 \sim T^n$, and the solid red line is fit to the spin-gap behavior $T^{\alpha}\exp(-\Delta_{flat}/T)$.

$\nu_0 = \gamma_N H_0$ is the unshifted Larmor frequency. The NMR shift comprises two contributions, $K(T) = K_0 + K_m(T)$. The first term is a chemical or orbital shift, which arises from the coupling with the Li electron density distribution. $K_m(T)$ is the magnetic shift resulting from the hyperfine coupling between the ^{7}Li nuclear spins and the Cr^{3+} spins. Shown in Fig. 5(b) is the temperature dependence of $K_m(T)$, which reflects the intrinsic magnetic susceptibility $\chi(T)$. With decreasing temperature through 5 K, the increment in $K_m(T)$ becomes enhanced. By correlating $K_m(T)$ with $\chi(T)$ with temperature being an implicit parameter, we estimate the dipolar hyperfine coupling A_{hf} between the ^{7}Li nuclear spins and the Cr^{3+} electron spins. In this so-called Clogston-Jaccarino $K_m - \chi$ plot, K_m is fitted using the equation

$$K_m(T) = K_0 + \left(\frac{A_{hf}}{N_A \mu_B}\right)\chi(T), \tag{4}$$

where N_A is Avogadro's number. Here, the zero intercept gives the chemical shift K_0. The $K_m - \chi$ fit in the $T = 5$–50 K range yields the hyperfine coupling constant $A_{hf} = 10.81\,\mathrm{mT}/\mu_B$ [see the inset of Fig. 5(b)]. As the temperature is lowered from 5 K, we observe a deviation from the linear $K_m - \chi$ relation, alluding to the presence of extrinsic effects.

Next, we turn to the ^{7}Li spin-lattice relaxation rate $1/T_1$, which conveys information about low-energy spin dynamics. The results are summarized in Figs. 5(c)–5(e). We first determined T_1^{str} by fitting $M(t)$ to the stretched exponential function. On cooling from $T = 30$ K, the stretched exponent $\beta(T) \approx 0.98$ exhibits a monotonic decrease to $\beta(T = 3\,\mathrm{K}) \approx 0.6$ [green squares in Fig. 5(d)], implying a substantial distribution of $1/T_1$ values at low temperatures. This together with the presence of two closely spaced ^{7}Li NMR lines renders it difficult to obtain reliable $1/T_1$ data. To overcome this, we employed the ILT method to analyze $M(t) = \sum_i P(1/T_{1i})[1 - \exp(-t/T_{1i})]$, where $P(1/T_{1i})$ represents the histogram of $1/T_{1i}$ subject to the condition $\sum_i P(1/T_{1i}) = 1$.

In Fig. 5(c), we present a cascade plot of $P(1/T_{1i})$ for selected temperatures at $T = 4$–20 K. A two-peak structure in $P(1/T_{1i})$ becomes discernible for temperatures below 20 K. By deconvoluting the $P(1/T_{1i})$ histogram into two Gaussian profiles, we obtain the temperature dependence of $1/T_{1s}$ (inverted green triangles) and $1/T_{1f}$ (pink triangles), as plotted in Fig. 5(e) on a log-log scale. It is worth emphasizing that T_1^{str} has a close overlap with the center of gravity (crosses) of $P(1/T_{1i})$, validating the accuracy of our ILT analysis. With lowering temperature below 50 K, $1/T_{1s}$ decreases continuously. We identify a power-law decrease $T^{1.58\pm0.04}$ in the $T = 3$–11 K interval. Notably, $1/T_2$ goes hand in hand with $1/T_{1s}$ in their thermal evolution [compare the diamonds in Fig. 5(d) with the inverted triangles in Fig. 5(e)]. This means that $1/T_2$ is governed by the $1/T_1$ mechanism. Further, we observe that $1/T_{1f}$ also displays a power-law dependence $T^{0.92\pm0.03}$ below T^*. Overall, the pseudogaplike suppression of $1/T_1$ below 50 K (in a paramagnetic state) is incompatible with their anticipated critical diverging behavior as $T \to T_C$, indicating that unconventional spin fluctuations are dictated by low-energy spin excitations.

In conventional ferromagnets, $1/T_1$ is dominated by the $\mathbf{q} = 0$ critical fluctuations that give rise to a critical increase

of $1/T_1 \sim T_r^{-p}$ as the temperature approaches T_C from a paramagnetic state. In the FM ordered state, however, $1/T_1$ is dictated by the scattering of magnons off nuclear spins, leading to power-law temperature dependences for temperatures larger than the spin-wave gap. Specifically, the spin-lattice relaxation rate exhibits a T^2 behavior with a logarithmic correction due to the Raman process and a $T^{7/2}$ behavior due to a three-magnon process [38]. Taken together, the intriguing temperature dependence of $1/T_1$ observed well above T_C cannot be captured by the aforementioned relaxation processes associated with acoustic magnons or paramagnons. In this situation, we recall that in kagome ferromagnets, a $\sqrt{3}\times\sqrt{3}$ magnetic superstructure emerges, and localized magnetic fluctuations develop on the hexagonal plaquette spins [21]. These fluctuations are pertinent to the optical flat magnon bands, and their effect is empirically described by the spin-gap formula $1/T_{1s} \sim T^{\alpha} \exp(-\Delta_{flat}/T)$. In the high-temperature range of $T = T^*$–40 K, where the critical slowing down is negligible, the gapped optical magnons provide a good description of $1/T_1$ with an effective spin gap of $\Delta_{flat} \approx 2.6J$ and $\alpha \approx 0.97$, as shown by the red line in Fig. 5(e). Here, we note that the effective spin gap is slightly smaller than the energy scale $3J$ of the flat magnon band [21]. As $\chi(T)$ shows no deviation from the CW behavior above 15 K [see the inset of Fig. 1(e)], the $\sqrt{3}\times\sqrt{3}$ mode mainly affects the dynamic ($\mathbf{q} \neq 0$) magnetic susceptibility. Further, $1/T_1$ switches to a power-law decrease through T^*, suggesting that other $1/T_1$ mechanisms come into play. Specifically, $\mathbf{q} = 0$ critical fluctuations, gapped magnons arising from the FM polarized state, and Dirac magnon bands may all contribute to $1/T_1$. Further investigations are needed to understand how all these sources result in a power-law decrease.

It is noteworthy that a similar NMR anomaly was observed in Cu_3TeO_6, which also hosts topological Dirac magnons [39]. We stress that our LCPP and Cu_3TeO_6 commonly feature topologically nontrivial flat optical magnon bands in addition to acoustic magnons. As such, the optical spin wave can serve as an additional relaxation channel on top of conventional relaxation mechanisms. Since a flat magnon band is defined on a hexagonal plaquette, it forms at a higher temperature than acoustic magnon bands. Consequently, certain short-range dynamics can appear at elevated temperatures, way higher than T_C.

IV. CONCLUSIONS

We have investigated the static and dynamical magnetic behavior of the kagome ferromagnet $Li_9Cr_3(P_2O_7)_3(PO_4)_2$ using magnetic susceptibilities, magnetization, specific heat, ESR, and ^{7}Li NMR. Magnetic susceptibility and specific heat showed a FM order below $T_C \sim 2.7$ K. The ferromagnetic correlation length extracted from $M(T, H)$ and spin dynamics determined by the ^{7}Li spin-lattice relaxation rate and the ESR linewidth evidenced that 2D magnetic correlations develop at much higher temperatures, up to $18T_C$, and the spin dynamics changes at $T^* \approx 4.4T_C$. The observed spin dynamics cannot be solely explained by $\mathbf{q} = 0$ critical fluctuations. Rather, gapped optical magnons dominate over low-energy spin excitations developing in the vicinity of the FM ordering vector at temperatures above T_C. Our study suggests that the thermal characteristics of spin dynamics in kagome ferromagnets are closely related to their magnon band structure. We call for further investigations to elucidate the relationship between the dynamical spin behavior and magnon band topology in kagome ferromagnets, as well as to test the presence of the magnon Hall effect.

ACKNOWLEDGMENTS

R.S. acknowledges financial support provided by the Ministry of Science and Technology in Taiwan under Projects No. MOST 111-2124-M-001-009, No. MOST 110-2112-M-001-065-MY3, and No. MOST 111-2124-M-A49-009 and Academia Sinica Project No. AS-iMATE-111-12. I.P.M. thanks the Banaras Hindu University for the Institutes of Eminence (IoE) Seed Grant. The work at SKKU is supported by the National Research Foundation (NRF) of Korea (Grants No. 2020R1A2C3012367 and No. 2020R1A5A1016518). The work at RIKEN is partially supported by JSPS KAKENHI Grant No. JP19K06606.

[1] P. A. McClarty, Topological magnons: A review, Annu. Rev. Condens. Matter Phys. **13**, 171 (2022).
[2] V. Bonbien, F. Zhuo, A. Salimath, O. Ly, A. Abbout, and A. Manchon, Topological aspects of antiferromagnets, J. Phys. D **55**, 103002 (2022).
[3] H. Katsura, N. Nagaosa, and P. A. Lee, Theory of the Thermal Hall Effect in Quantum Magnets, Phys. Rev. Lett. **104**, 066403 (2010).
[4] R. Matsumoto and S. Murakami, Theoretical Prediction of a Rotating Magnon Wave Packet in Ferromagnets, Phys. Rev. Lett. **106**, 197202 (2011).
[5] L. Zhang, J. Ren, J.-S. Wang, and B. Li, Topological magnon insulator in insulating ferromagnet, Phys. Rev. B **87**, 144101 (2013).
[6] R. Shindou, R. Matsumoto, S. Murakami, and J.-I. Ohe, Topological chiral magnonic edge mode in a magnonic crystal, Phys. Rev. B **87**, 174427 (2013).
[7] E. G. Mishchenko and O. A. Starykh, Equilibrium currents in chiral systems with nonzero Chern number, Phys. Rev. B **90**, 035114 (2014).
[8] A. Mook, J. Henk, and I. Mertig, Magnon Hall effect and topology in kagome lattices: A theoretical investigation, Phys. Rev. B **89**, 134409 (2014).
[9] S. A. Owerre, A first theoretical realization of honeycomb topological magnon insulator, J. Phys.: Condens. Matter **28**, 386001 (2016).
[10] S. A. Owerre, Topological thermal Hall effect in frustrated kagome antiferromagnets, Phys. Rev. B **95**, 014422 (2017).
[11] P. Laurell and G. A. Fiete, Magnon thermal Hall effect in kagome antiferromagnets with Dzyaloshinskii-Moriya interactions, Phys. Rev. B **98**, 094419 (2018).
[12] S. S. Pershoguba, S. Banerjee, J. C. Lashley, J. Park, H. Ågren, G. Aeppli, and A. V. Balatsky, Dirac Magnons in Honeycomb Ferromagnets, Phys. Rev. X **8**, 011010 (2018).

[13] K.-S. Kim, K. H. Lee, S. B. Chung, and J.-G. Park, Magnon topology and thermal Hall effect in trimerized triangular lattice antiferromagnet, Phys. Rev. B **100**, 064412 (2019).

[14] Y. Lu, X. Guo, V. Koval, and C. Jia, Topological thermal Hall effect driven by spin-chirality fluctuations in frustrated antiferromagnets, Phys. Rev. B **99**, 054409 (2019).

[15] A. Mook, J. Henk, and I. Mertig, Thermal Hall effect in noncollinear coplanar insulating antiferromagnets, Phys. Rev. B **99**, 014427 (2019).

[16] F. Zhuo, H. Li, and A. Manchon, Topological phase transition and thermal Hall effect in kagome ferromagnets, Phys. Rev. B **104**, 144422 (2021).

[17] R. R. Neumann, A. Mook, J. Henk, and I. Mertig, Thermal Hall Effect of Magnons in Collinear Antiferromagnetic Insulators: Signatures of Magnetic and Topological Phase Transitions, Phys. Rev. Lett. **128**, 117201 (2022).

[18] Y. Onose, T. Ideue, H. Katsura, Y. Shiomi, N. Nagaosa, and Y. Tokura, Observation of the magnon Hall effect, Science **329**, 297 (2010).

[19] T. Ideue, Y. Onose, H. Katsura, Y. Shiomi, S. Ishiwata, N. Nagaosa, and Y. Tokura, Effect of lattice geometry on magnon Hall effect in ferromagnetic insulators, Phys. Rev. B **85**, 134411 (2012).

[20] M. Hirschberger, R. Chisnell, Y. S. Lee, and N. P. Ong, Thermal Hall Effect of Spin Excitations in a Kagome Magnet, Phys. Rev. Lett. **115**, 106603 (2015).

[21] R. Chisnell, J. S. Helton, D. E. Freedman, D. K. Singh, R. I. Bewley, D. G. Nocera, and Y. S. Lee, Topological Magnon Bands in a Kagome Lattice Ferromagnet, Phys. Rev. Lett. **115**, 147201 (2015).

[22] R. Chisnell, J. S. Helton, D. E. Freedman, D. K. Singh, F. Demmel, C. Stock, D. G. Nocera, and Y. S. Lee, Magnetic transitions in the topological magnon insulator Cu(1,3-bdc), Phys. Rev. B **93**, 214403 (2016).

[23] H. Takeda, J. Mai, M. Akazawa, K. Tamura, J. Yan, K. Moovendaran, K. Raju, R. Sankar, K.-Y. Choi, and M. Yamashita, Planar thermal Hall effects in the Kitaev spin liquid candidate $Na_2Co_2TeO_6$, Phys. Rev. Res. **4**, L042035 (2022).

[24] D. L. Bergman, C. Wu, and L. Balents, Band touching from real-space topology in frustrated hopping models, Phys. Rev. B **78**, 125104 (2008).

[25] M. Pereiro, D. Yudin, J. Chico, C. Etz, O. Eriksson, and A. Bergman, Topological excitations in a kagome magnet, Nat. Commun. **5**, 4815 (2014).

[26] F. Zhuo, H. Li, and A. Manchon, Topological thermal Hall effect and magnonic edge states in kagome ferromagnets with bond anisotropy, New J. Phys. **24**, 023033 (2022).

[27] S. Poisson, F. d'Yvoire, N. Guyen-Huy-Dung, E. Bretey, and P. Berthet, Crystal structure and cation transport properties of the layered monodiphosphates: $Li_9M_3(P_2O_7)_3(PO_4)_2$ (M = Al, Ga, Cr, Fe), J. Solid State Chem. **138**, 32 (1998).

[28] A. Magar, S. K. V. Singh, J. J. Abraham, Y. Senyk, A. Alfonsov, B. Büchner, V. Kataev, A. A. Tsirlin, and R. Nath, Large Magnetocaloric Effect in the Kagome Ferromagnet, Phys. Rev. Appl. **18**, 054076 (2022).

[29] P. M. Singer, A. Arsenault, T. Imai, and M. Fujita, ^{139}La NMR investigation of the interplay between lattice, charge, and spin dynamics in the charge-ordered high-T_c cuprate $La_{1.875}Ba_{0.125}CuO_4$, Phys. Rev. B **101**, 174508 (2020).

[30] C. Lee, S. Lee, Y. S. Choi, C. Wang, H. Luetkens, T. Shiroka, Z. H. Jang, Y.-G. Yoon, and K.-Y. Choi, Coexistence of random singlets and disordered Kitaev spin liquid in $H_3LiIr_2O_6$, Phys. Rev. B **107**, 014424 (2023).

[31] S. J. Sebastian, K. Somesh, M. Nandi, N. Ahmed, P. Bag, M. Baenitz, B. Koo, J. Sichelschmidt, A. A. Tsirlin, Y. Furukawa, and R. Nath, Quasi-one-dimensional magnetism in the spin-$\frac{1}{2}$ antiferromagnet $BaNa_2Cu(VO_4)_2$, Phys. Rev. B **103**, 064413 (2021).

[32] A. Abragam and B. Bleaney, *Electron Paramagnetic Resonance of Transition Ions* (Oxford University Press, Oxford, 2012).

[33] S. Lee, S.-H. Do, W.-J. Lee, Y. S. Choi, M. Lee, E. S. Choi, A. P. Reyes, P. L. Kuhns, A. Ozarowski, and K.-Y. Choi, Multistage symmetry breaking in the breathing pyrochlore lattice Li(Ga, In)Cr_4O_8, Phys. Rev. B **93**, 174402 (2016).

[34] *Magnetic Properties of Layered Transition Metal Compounds*, edited by L. J. De Jongh (Springer, Dordrecht, 1990).

[35] R. Klingeler, B. Büchner, S.-W. Cheong, and M. Hücker, Weak ferromagnetic spin and charge stripe order in $La_{5/3}Sr_{1/3}NiO_4$, Phys. Rev. B **72**, 104424 (2005).

[36] D. Boldrin, B. Fåk, M. Enderle, S. Bieri, J. Ollivier, S. Rols, P. Manuel, and A. S. Wills, Haydeeite: A spin-$\frac{1}{2}$ kagome ferromagnet, Phys. Rev. B **91**, 220408(R) (2015).

[37] M. Jonak, E. Walendy, J. Arneth, M. Abdel-Hafiez, and R. Klingeler, Low-energy magnon excitations and emerging anisotropic nature of short-range order in CrI_3, Phys. Rev. B **106**, 214412 (2022).

[38] D. Beeman and P. Pincus, Nuclear spin-lattice relaxation in magnetic insulators, Phys. Rev. **166**, 359 (1968).

[39] S.-H. Baek, H. W. Yeo, J. Park, K.-Y. Choi, and B. Büchner, Unusual spin pseudogap behavior in the spin web lattice Cu_3TeO_6 probed by ^{125}Te nuclear magnetic resonance, Phys. Rev. Res. **3**, 033109 (2021).